Addressing Spatial Variability of Surface-Layer Wind with Long-Range WindScanners

Berg, Jacob; Vasiljevic, Nikola; Kelly, Mark C.; Lea, Guillaume; Courtney, Michael

Published in:
Journal of Atmospheric and Oceanic Technology

Link to article, DOI:
10.1175/JTECH-D-14-00123.1

Publication date:
2015

Document Version
Publisher's PDF, also known as Version of record

Addressing Spatial Variability of Surface-Layer Wind with Long-Range WindScanners

JACOB BERG, NIKOLA VASILJEVÍC, MARK KELLY, GUILLAUME LEA, AND MICHAEL COURTNEY

Department of Wind Energy, Technical University of Denmark, Roskilde, Denmark

(Manuscript received 23 June 2014, in final form 9 December 2014)

ABSTRACT

This paper presents an analysis of mean wind measurements from a coordinated system of long-range WindScanners. From individual scan patterns the mean wind field was reconstructed over a large area, and hence it highlights the spatial variability. From comparison with sonic anemometers, the quality of the WindScanner data is high, although the fidelity of the estimated vertical velocity component is significantly limited by the elevation angles of the scanner heads. The system of long-range WindScanners presented in this paper is close to being fully operational, with the pilot study herein serving not only as a proof of concept but also verifying expectations of reliable wind measurements over arbitrary three-dimensional volumes, in future sustained meteorological campaigns.

1. Introduction

Conventionally, winds in the atmospheric boundary layer are measured by mast-mounted cup or sonic anemometers. Today this picture is heavily challenged by remote sensing instruments, such as sodars and especially lidars (Emeis et al. 2007). Whereas the mast-mounted instruments (mainly sonics) are still superior when it comes to measuring and quantifying turbulent structures (Sathe et al. 2011), the advantages of remote sensing instruments are obvious: easy deployment for campaigns with a flexible layout, a fixed coordinate system for profile studies (Berg et al. 2013), measurements above the surface layer (Peña et al. 2009), detailed wake studies (Bingöl et al. 2010; Trujillo et al. 2011; Smalikho et al. 2013; Aitken et al. 2014), offshore applications, (Peña et al. 2010), etc.

Doppler lidars are often used for studies of the atmospheric surface layer and above. The line-of-sight velocity is recorded as proportional to the Doppler-shifted aerosol backscatter. By performing a velocity–azimuth display (VAD) scan, the horizontal velocity can be determined, assuming horizontal homogeneity (Browning and Wexler 1968). For horizontally heterogeneous conditions, the single-lidar VAD scan is not a possibility. Bingöl et al. (2009) estimated the error when using a lidar in moderately complex terrain and dictated a road ahead using flow models for correcting the lidar results. In very complex terrain, flow models, however, have their own problems (Bechmann et al. 2011), and therefore a model-independent method is needed. A system of multiple lidars is perhaps the best solution when addressing heterogeneity and spatial variability. Mayor and Eloranta (2001) used a volume imaging lidar (VIL), a non-Doppler single-scanning aerosol backscatter lidar using a cross-correlation technique to measure spatial-varying wind fields with a resolution of 250 m, and as such were able to detect large-scale phenomena such as sea breezes. Newsom et al. (2008) applied two Doppler lidars in coordinated plan position indicator (PPI) scans with a small elevation angle over an area approximately 2 km × 2 km with a resolution of 100 m. The authors were able to see elongated two-dimensional turbulent structures in the plane along the laser beams. Range–height indicator (RHI) scans were also performed.

These two experiments had the lidars performing either pure PPI or RHI scans. They therefore had a limited number of degrees of freedom and hence applicability. In addition, only two-dimensional velocity vectors were retrieved. To obtain even more information about the wind field, the next step could be a system consisting of three lidars, so that the full 3D velocity vector in time can be obtained using programmable scanning trajectories with infinite degrees of

Corresponding author address: Jacob Berg, Department of Wind Energy, Technical University of Denmark, Risø Campus, Frederiksborgvej 399, 4000 Roskilde, Denmark.
E-mail: jbej@dtu.dk

DOI: 10.1175/JTECH-D-14-00123.1

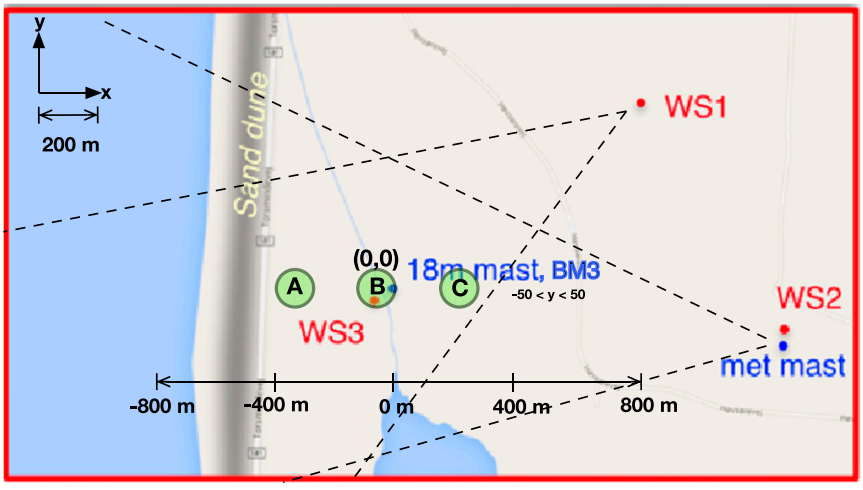

FIG. 1. Map of test site. The 18- and 116-m meteorological masts are indicated with blue dots, and the WindScanner positions are indicated with red dots; dotted lines represent boundaries for the TV scans from WS1 and WS2 (see Fig. 4). Green circles A–C indicate measurement areas used for the calculations of section 5.

freedom. This paper will present data from such a system of three spatially separated, long-range, coherent Doppler scanning lidars (WindScanners) that can address the issue of spatial variability due to inhomogeneity by collectively moving the three beams to follow any desired trajectory; that is, there is no restriction to perform only pure PPI or RHI scans.

Prior to the campaign documented herein, a series of measurements were performed. In the ''Swinging Musketeer'' experiment (Vasiljević 2014), the same system of WindScanners utilized here was steered toward three sonic anemometers positioned at different heights (76, 94, and 118 m). During 6 h, the difference between the three components of velocity obtained from the sonics and the WindScanners averaged over 1 min was less than 0.1 m s^{-1}. We have therefore obtained confidence in the new system of WindScanners and want to demonstrate it in a more realistic setting; a setting in which the spatial scales are larger, and we therefore have to design much more complex scan patterns. This is the focus of the current paper, where the system of WindScanners is deployed at the Danish Test Center for Large Wind Turbines at Høvsøre, Denmark, and a field campaign is performed. The main focus is to test and benchmark the system of WindScanners in contrast to establishing new relationships within boundary layer meteorology. The former has not previously been documented in the literature.

In section 2 we present the setup of the field campaign. The meteorological conditions, during the two days from which data are presented, are briefly discussed in section 3. In section 4 the method by which we retrieve velocities is presented, and a comparison with a fixed mounted sonic anemometer is performed. In section 5 we present results on spatial variability. The conclusions finalize the paper.

2. Setup

We performed a measurement campaign at the Test Center for Large Wind Turbines, at Høvsøre on the western Danish coast, in June 2013. The layout and infrastructure of the test site have been used for numerous studies (Courtney et al. 2008; Berg et al. 2013; Peña et al. 2014).

As shown in Fig. 1, the site is ~1–2 km east of the North Sea. Two meteorological masts are utilized: a 116-m meteorological mast to the east and an 18-m mast, BM3, in the center of the domain. The three WindScanners are denoted as WS1, WS2, and WS3, respectively. Worth noting is the sand dune running roughly south–north and separating the beach from the farmland to the east; its height (varying locally in space), approximately 16 m, cannot be neglected for westerly winds. The remainder of the terrain is flat, mostly consisting of farmland and with some trees and bushes farther from the center of the domain.

The campaign lasted approximately three weeks. In this contribution we will, however, only present data from two full days (from 1650 UTC 17 June to 1350 UTC 19 June) in which the three WindScanners were running with almost no interruptions and in scan configurations favorable for studies of spatial variability. Two days of data are surely not enough to study the meteorological

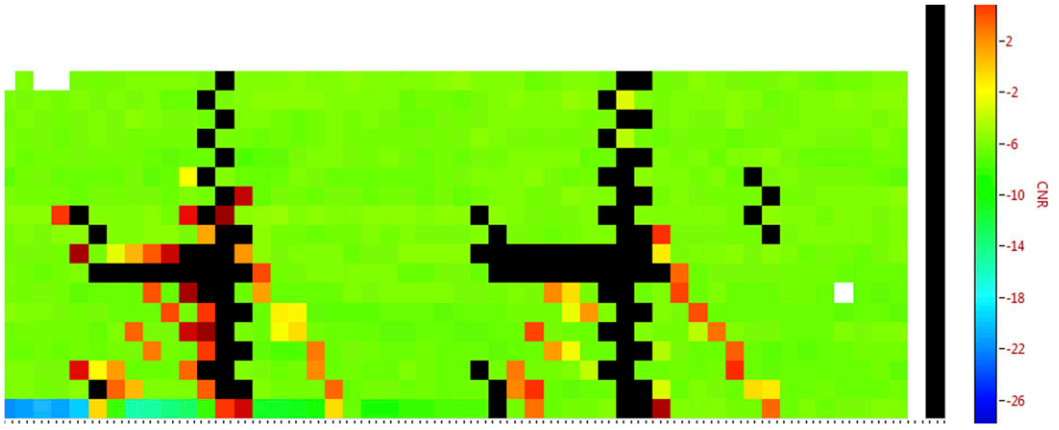

FIG. 2. BM3 is used as a hard target. Here observed from WS1 (left figure) and WS2 (right figure) through carrier-to-noise mapping. Distance is depicted on the horizontal axis. No units are given, since the perspective is due to different azimuthal angles between WS1 and WS2 to BM3.

signature in greater detail, but it is large enough to establish a proof of concept of the current setup of WindScanners.

a. *WindScanner configurations*

The WindScanners are the newly developed 1543-nm coherent Doppler scanning lidars at Technical University of Denmark (DTU) Wind Energy; these are based on the pulsed lidar Windcube 200 from Leosphere, plus a dual-axis mirror-based steerable scanner head designed by DTU Wind Energy and the Danish innovation factory IPU.

The three WindScanners are coordinated using a remote master computer. As such, the three lidars together with the master computer form a unique measurement system that is able to measure a complete three-dimensional flow field by emitting laser beams and directing them to intersect within a volume of interest; each lidar uses an industrial motion controller to control the laser pulse emission and steering, and the acquisition of the backscattered light. The lidar software provides the means to set up arbitrary scanning trajectories and the distribution of the distances at which radial velocity is retrieved (range gates) for any given line-of-sight measurement, and to control the time during the measurements. Particularly, the ability to control time and the ability to create arbitrary trajectories are, to our knowledge, not provided by any other existing scanning lidar.

Very high beam position accuracy is achieved by using hard targets for calibration through signal-to-noise mapping. In this particular case, we have used the mast BM3. In Fig. 2 WS1 and WS2 are looking at BM3. We can clearly see both the mast and a boom with a sonic as well as the wires.

The simultaneous coordination of the WindScanners via the master computer is achieved through communication with a user datagram protocol/Internet protocol (UPD/IP) and transmission control protocol/Internet protocol (TCP/IP) network. The network communication is defined by a newly developed remote sensing communication protocol (Vasiljević et al. 2013b). The centralized coordination of multiple scanning lidars is necessary in order to achieve full synchronization between the lidars (Vasiljević et al. 2013a). In the Swinging Musketeer experiment, we showed that we can achieve synchronized down to a few milliseconds (Vasiljević 2014).

An example of a full 360° PPI scan (not part of the analysis of this paper) from WS1 is given in Fig. 3. The elevation angle is 4° and the speed is $1°\,s^{-1}$ with range gates set every 50 m out to a radius of 5 km. While wakes from the nearby wind turbines from the Test Center for Large Wind Turbines are clearly visible, the interface between land and sea is not, since this relatively small signal drowns in the much larger variation in the radial speeds (due to the changing height and projection angle) that we are examining. However, from the change in sign of the radial speeds, we can clearly determine the northwesterly wind direction.

b. *WindScanner configurations*

In contrast to the data shown in Fig. 3, which are radial wind speeds measured from a single lidar, in the remainder of this paper, we will be concerned with wind speeds derived from combining the WindScanner system's three radial wind speeds. The scan patterns of the three WindScanners are illustrated in Fig. 4, with angular ranges (scan geometries) provided in the caption. The scans are designed to focus on the area around the

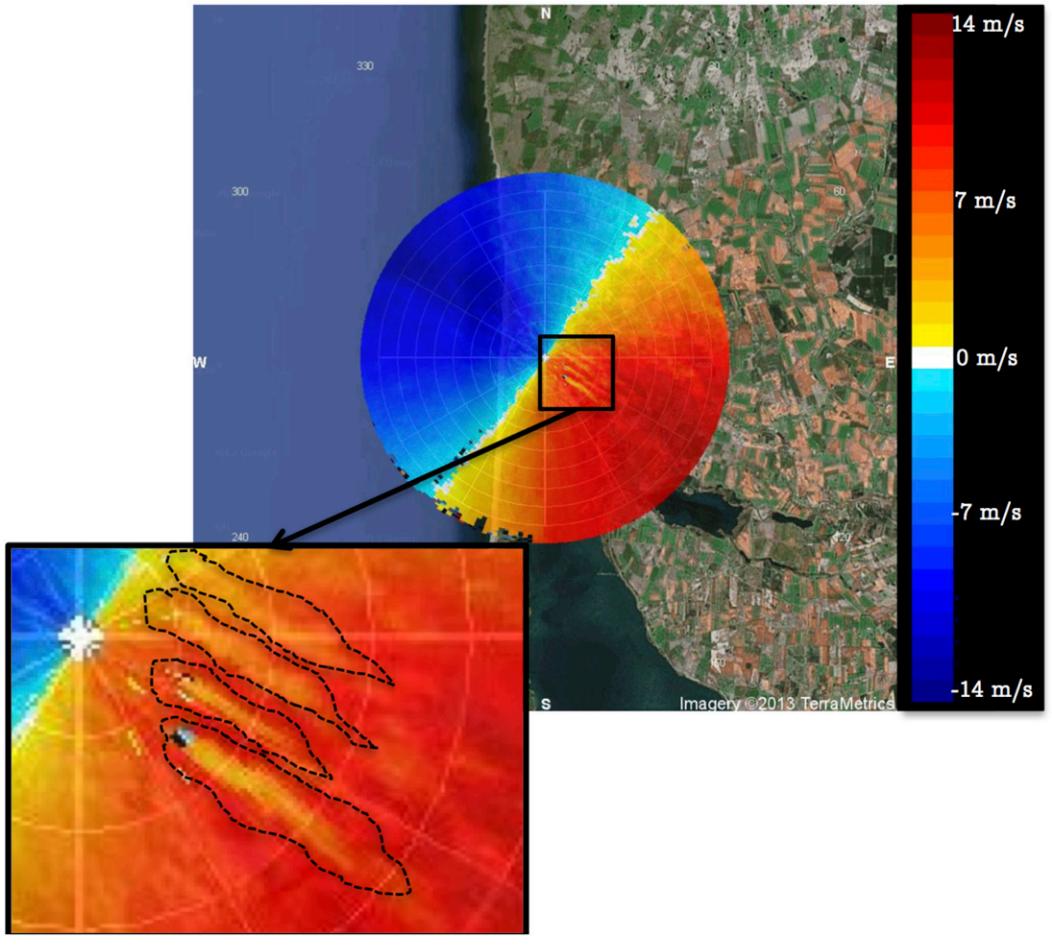

FIG. 3. An example of a 360° PPI scan from WS1. Turbine wakes are highlighted in the inset.

coordinate system's origin, $\{x, y\} = \{0, 0\}$. WS1 and WS2 were fully synchronized in so-called TV-scan modes, where straight lines along the y direction are scanned at five different heights (left and middle panels). To do so, both the elevation and azimuthal angles are varied simultaneously, and the scan is therefore not just consecutive PPI scans for various elevation angles. Furthermore, the positions of the individual range gates are changed between the different line-of-sight beam positions corresponding to a given set of elevation and azimuthal angles. A full cycle took 35 s. In contrast, WS3 was operated in a so-called flower-scan mode (right panel), where five consecutive 180° RHI scans were performed for different azimuthal angles. Because of the large number of discrete angles sampled, the scanner head used 65 s to complete a full cycle. The

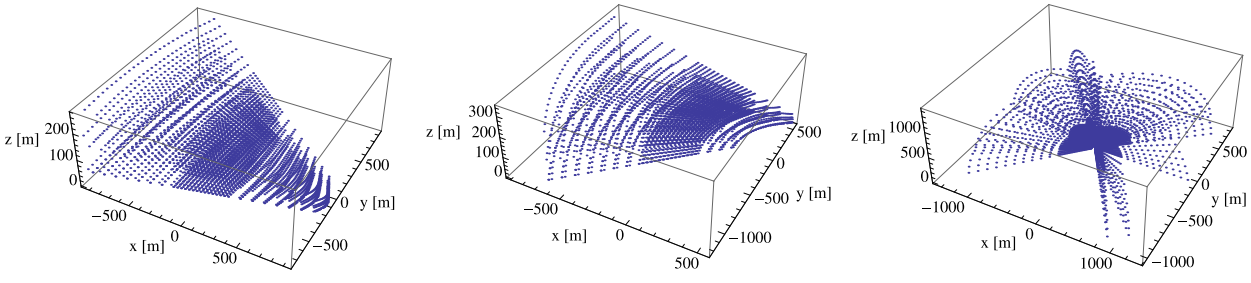

FIG. 4. (left to right) WindScanner configurations for WS1–WS3 from 1650 UTC 17 Jun to 1350 UTC 19 Jun. The range of azimuthal angles are 240°–300°, 220°–260°, and 54°–136°, the elevation angles are 1°–7°, 0°–12°, and 0°–180°, and the number of range gates are {29, 25, 30}, respectively. The scan cycles take 35, 35, and 65 s, respectively.

WindScanners emitted laser pulses with a temporal length of 200 ns, corresponding to an effective sampling length of about 30 m along the beam. The pulses were streamed with a pulse repetition frequency of 20 kHz, and each laser pulse contained 50 μJ of energy. The measurement rate was 5 Hz, and the number of range gates was 25 (WS3) and 30 (WS1–2).

We have used data based on the individual WindScanner signal-to-noise ratios (accepting data between −10 and −23 dB). In addition, we discovered serious errors in the output of the maximum-likelihood estimator (MLE) of WS3, which we managed to link to the field-programmable gate array (FPGA; acquisition) board. The error affected both the spectral broadening of the received signal, the signal-to-noise ratios, and the line-of-sight velocities. We found a tendency that the spurious line-of-sight velocities occurred in the left tail of the distributions of spectral broadening (dispersion). These unrealistically small values are due to the system locking between consecutive range gates—hence, a constant return spectrum for the different range gates. To reject the affected measurements, the distributions of spectral broadening were truncated, and only measurements with a spectral broadening larger than the truncation value have been used in the analysis.

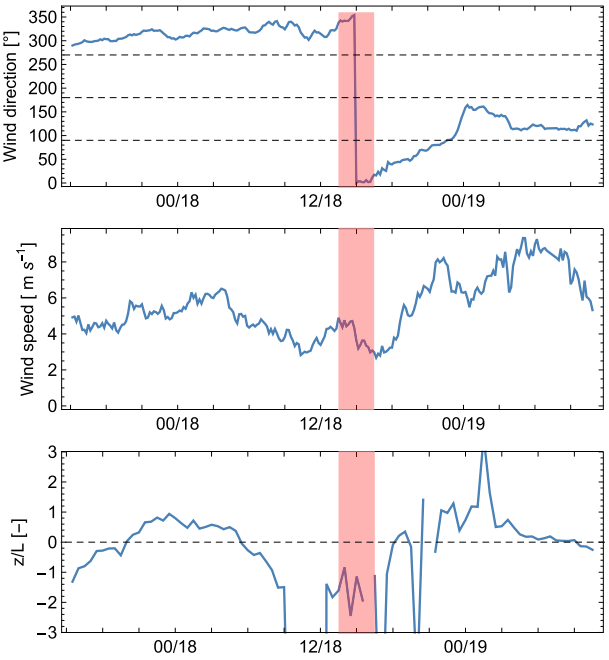

FIG. 5. Time series (from 1500 UTC 17 Jun 2013 to 1100 UTC 19 Jun 2013) measured from the 116-m meteorological mast. Wind speed and direction are measured at 80 m, and the stability parameter z/L is measured at 20 m. Here L is the Obukhov length, so that $z/L < 0$ denotes convective conditions, while $z/L > 0$ denotes stable conditions. The red area indicates the time interval not used in the analysis presented in section 5.

3. Meteorological setting

With westerly winds the internal boundary layers arising from both the coastline and the sand dune can in principle be studied. In Fig. 5 we present some time series of wind speed, wind direction, and stability parameter, z/L, from the "tall" (116 m) meteorological mast. The Obukhov length L is defined in the usual way (see, e.g., Wyngaard 2010).

Looking at the time series, we see that northwesterly wind prevails until around 1400 UTC 18 June, with strong convection indicated by highly negative z/L values and low wind speed. Later, the wind speed increases again, and the wind direction changes to easterly directions with stably-stratified or neutral conditions. In this study (section 5) we will split the dataset into two pieces, that is, before and after the red shaded area. We thus analyze two periods with different wind direction, westerly and easterly, but with roughly the same distribution of z/L. Only the small time interval around wind from true north is avoided, because the periods are neither easterlies nor westerlies (the highlighted interval in Fig. 5).

4. Averaging WindScanner data

The three WindScanners were used in a semi-synchronized manner: WS1 and WS2 made collocated planar TV scans at the same scan cycle frequency, while WS3 used approximately twice as long for its flower-scan cycle (Fig. 4). Such an operation was chosen primarily in order to optimize the temporal resolution. Fully synchronizing the WindScanners demands that they "wait" for each other; because of the size of the scan area, a complete cycle would therefore take a longer amount of time. The drawback is that the three beam positions never coincided at the exact same position in time. We are therefore not able to reproduce the three-dimensional turbulent time series of high resolution. Instead, we focus on the mean wind, defined as an average in four dimensions.

We define three-dimensional volumes ($\Delta x \Delta y \Delta z$) over time intervals Δt. To estimate the mean at a point $\{x, y, z\}$ and time t, we take all beam positions from the three WindScanners falling within a space–time volume defined by $\{[x \pm \Delta x/2], [y \pm \Delta y/2], [z \pm \Delta z/2], [t; t + \Delta t]\}$.

In the following we will use i to denote the index of the WindScanner, j to denote the particular velocity component, $u_j = \{u, v, w\}$, and let the angle brackets $\langle \cdot \rangle$ denote volume averages. If all three WindScanners have a beam position within the same space–time box, then the mean velocity vector, $U_j \equiv \langle u_j \rangle$, can be calculated by solving the linear system of equations

$$M_{ij}\, U_j = U_{\mathrm{los},i} \tag{1}$$

for U_j. Here $U_{\mathrm{los},i} \equiv \langle u_{\mathrm{los},i} \rangle$ is the mean line-of-sight velocity vector for the ith WindScanner, and the ith entry of M_{ij} is given by

$$M_i = \{\langle \sin\phi_i \cos\theta_i \rangle, \langle \cos\phi_i \cos\theta_i \rangle, \langle \sin\theta_i \rangle\}, \tag{2}$$

where ϕ is the azimuthal angle and θ is the elevation angle (positive above ground). The ranges of ϕ and θ are given in the caption of Fig. 4. To minimize numerical errors for ill-conditioned matrices due to nonoptimal beam configurations (for low elevations the vertical velocity is poorly resolved), we use lower–upper (LU) decomposition with pivoting when solving Eq. (1) for U_j (Strang 2005).

To study the influence of the 4D averaging volume defined above (toward obtaining robust results), given the spatial averaging implicit in lidar use (Sathe and Mann 2013), we compare the WindScanners with a sonic anemometer mounted on the top of the $z = 18$ m mast, BM3, located between the three WindScanners (cf. Fig. 1).

The wind components u, v, and w are taken along the east–west, south–north, and vertical directions, respectively. Three configurations, with different spatial dimensions, are presented. We use $\Delta t = 10$ min and calculate via cylinders of horizontal radius ΔR and height Δz, centered around BM3 at (0, 0, 18 m). The main results are presented in Fig. 6 for the three configurations, where ($\Delta R = 15$ m, $\Delta z = 6$ m) is represented by the red curves, ($\Delta R = 25$ m, $\Delta z = 12$ m) is represented by the green curves, and ($\Delta R = 50$ m, $\Delta z = 12$ m) is represented by the blue curves. This gives the beam center positions (in meters) of $\{-5.1 \pm 1.9, -3.8 \pm 0.8, 17.9 \pm 0.1\}$ for red, $\{0.9 \pm 5.0, -1.1 \pm 3.9, 18.4 \pm 1.6\}$ for green, and $\{-6.6 \pm 12.2, 0.4 \pm 8.7, 18.5 \pm 1.5\}$ for blue.

For the two horizontal wind components, u and v, the agreement with the sonic anemometer is in general quite good (except for northerly wind directions, where the mast causes flow distortion). The worst agreement is the smallest volume (red curve), which is counterintuitive—because of the larger spread of data points in the larger volume configurations, and a distance to the sand dune of only 350 m. This may be explained by the smaller number of data points sampled compared to the larger volumes (green and blue lines). The outcome is reversed for the vertical component w, which is associated with smaller spatial scales: an increased number of spurious fluctuations are captured in the larger volumes (green and blue curves). However, none of the configurations provide data quality sufficient for calculation of tilt angles with any confidence. We attribute this to the WindScanner configuration, where two of the WindScanners (WS1, WS2) are located a large distance away and in almost the same horizontal plane, for the low elevation angles set here. Given the comparison in the two top panels of Fig. 6, we conclude that the horizontal velocities of the lidars and sonic are similar, and hence we can use the system to study the spatial viability of the areas highlighted in Fig. 4.

A consequence of the use of unsynchronized WindScanners with the averaging method described in this section is that it is not possible to quantify turbulence in the usual setting of $\{\sigma_u, \sigma_v, \sigma_w\}$; with scan cycles of 35, 35, and 65 s, respectively, the temporal resolution is too coarse. It is, however, possible to study the variations of the line-of-sight velocities from the different range gates and from that get an indication of the turbulence level (not part of this paper).

5. Spatial variability

Based on the comparison with the sonic at 18 m mounted on mast BM3, we choose $\Delta R = 50$ m and $\Delta z = 12$ m to analyze the mean wind field. With a distance of approximately 600 m to the seashore, we do not have any intersecting beams over the sea. The sand dune is located approximately between $x = -500$ and $x = -400$, and the lowest elevation angles are chosen, so that the dunes are not in the line of sight of any of the WindScanners.

In Fig. 7 we show 30-min averages of the horizontal wind in the x–z plane. The plot is composed of averages along the x axis and ± 50 m to the north and south of it. Because of the pattern of beam crossings, there are missing points. We have therefore used linear interpolation to cover the full area where possible, even though this might introduce small errors in the patterns, as, for example, the straight contour lines observed. The uneven coverage in the four panels suggests many missing data to the west (to the left in the panels). The two top panels are for the westerly wind regime, while the bottom ones are from the easterly subset. In the cases with unstable stratification (left panels), a layered structure is visible, but with only a small variation of wind speeds. This is in contrast to the stable cases, where especially for easterly winds (bottom-right panel), the range of wind speeds is much higher and the layered vertical structure is much more pronounced. For stable westerlies (top-right panel), the presence of the sand dune is observed, with slightly lower wind speeds extending to 125-m height just downstream from the dune. The well-known stratified structure is recovered again downstream for $x \gtrsim -200$ m. The impact of the dune on the horizontal mean wind can also be observed in the unstable case (top-left panel) although it is somewhat

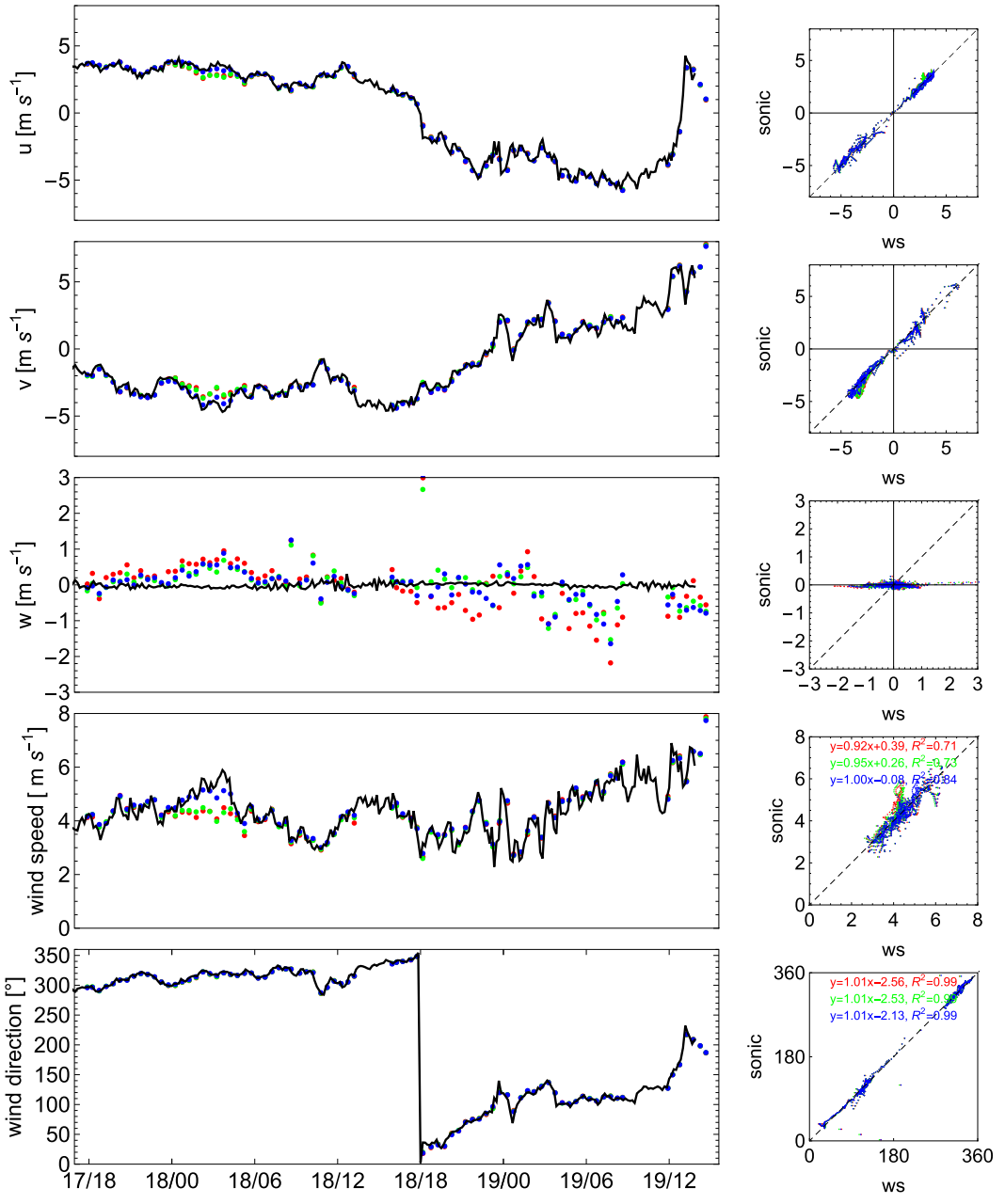

FIG. 6. Time series: sonic anemometer at mast BM3 at $z = 18$ m (black) and WindScanners with $\{\Delta R, \Delta z\}$ of {15 m, 6 m} (red), {25 m, 12 m} (green), and {50 m, 12 m} (blue). Linear fit model parameters are included for the wind speed and wind direction.

weaker. The dune's effect is to disrupt the internal boundary layer formed at the sea–land interface. For stable westerly flows there does, however, appear to be a sloping gradient extending from $\{x, z\} \approx \{-400, 50\}$ m to $\{x, z\} \approx \{-200, 200\}$ m; unfortunately, this is also the boundary for which we have data.

An interesting question, namely, to which degree does the sand dune induce turbulence and promote adjustment of the flow to the onshore roughness—that is, through vertical mixing—in different stabilities, is hard to answer from these measurements alone.

We have also calculated the correlation coefficient,

$$\rho_{\alpha\beta} = \frac{\mathrm{cov}[U(x_\alpha, z; t), U(x_\beta, z; t)]}{\sigma_U(x_\alpha, z)\sigma_U(x_\beta, z)}, \tag{3}$$

between pairs of time series of horizontal wind speed measured at height z above ground, separated by

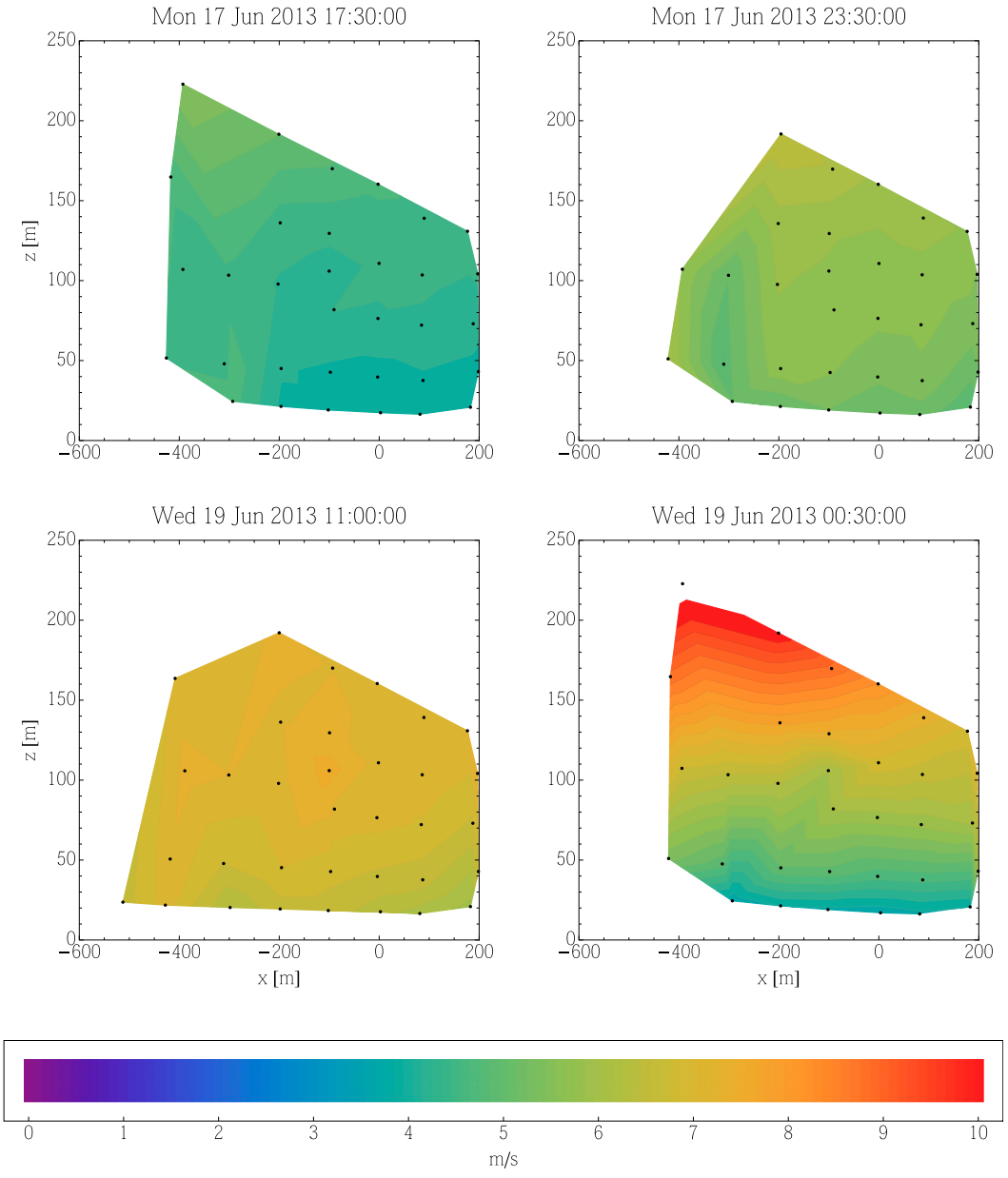

FIG. 7. Temporal snapshots of the 30-min averaged horizontal wind along the x axis at $y = 0 \pm 50$ m. The snapshots are taken at (top) westerly wind directions and (bottom) easterly wind directions in (left) unstable and (right) stable stratification. The dots indicate the actual measurement points. Linear interpolation is used to connect the dots.

a distance $|x_\beta - x_\alpha|$ in the east–west direction. This was done using the points A, B, and C, presented in Fig. 1, whose locations have corresponding x coordinates of -300, -50, and 200 m, respectively; all have $y = 0$ m. The three points were chosen where three beams were overlapping and the data retrieval and quality were high.

Since we are limited to time series of less than a day for each of the two wind directions, we are thus dealing with the so-called terra incognita between turbulence and mesoscale motions (Wyngaard 2004); hence, the determination of characteristic time scales is not straightforward.

For westerly winds, at 10 m AGL we find $\rho_{AB} = 0.48$, $\rho_{AC} = 0.47$, and $\rho_{BC} = 0.87$. The higher correlation between points B and C suggests that at $z = 10$ m, and that the flow has recovered from the effect of the dune ($x = -400$ m) by the time it reaches point B, that is, over a span of ~350 m or less; this interpretation is supported by our finding that for easterly winds, the correlation is

the same: $\rho_{CB}|_{z=10m} = 0.87$. Because there is only flat land to the east, we see relatively higher correlations closer to the dune for easterly flow ($\rho_{BA} = 0.87$, $\rho_{CA} = 0.78$) than for westerly flow ($\rho_{AB} = 0.48$, $\rho_{AC} = 0.47$).

Higher above the ground but still well within the ABL, the pairwise correlations are expected to be larger than those at $z = 10$ m. Indeed, at $z = 95$ m, for the westerly regime we find $\rho_{AB} = 0.60$, $\rho_{AC} = 0.68$, and $\rho_{BC} = 0.91$, whereas for the easterly regime we find $\rho_{BA} = 0.95$, $\rho_{CA} = 0.91$, and $\rho_{CB} = 0.91$. This is due to the relatively smaller influence of the ground, and we note that subsequently the dune reduces the correlations involving point A relatively less than at $z = 10$ m. The coastline several hundred meters to the west does not appear to *directly* affect the statistics presented here, since the corresponding perturbations of the offshore inflow (i.e., internal boundary layer) are dominated ("mixed away") by the dune-induced boundary layer. One can see some evidence for this in Fig. 7, though under stable enough conditions, such an assumption may begin to fail; this is left for further research.

6. Conclusions

We have presented data from a system of long-range WindScanners, demonstrating that with the present configuration it is possible to obtain valuable information about the mean wind flow. Even though the area studied in this paper is not to be considered *large*, the system facilitates the scanning of much larger areas. There will always be a trade-off between the length or detail of the scanning trajectories (spatial resolution) and the duration of the scan cycles (temporal resolution).

Turbulence can be studied in two ways with the current system—either temporally with fast short scan cycles or spatially with longer slower trajectories. In both cases we would need the three WindScanners to operate in a fully time-synchronized mode, which is indeed possible, since this would allow for the estimation of all three velocity components at the exact same time and position. Information about the spatial coherence (Mann 1994) could then be obtained (work in progress).

To obtain longer uninterrupted time series for data analysis in the context of micrometeorology, there are still some system components that need development; in particular, the maximum-likelihood estimator (MLE) is being refined to permit online detection of spurious data in future campaigns. Also under development is software to automate the generation of complex synchronized trajectories, such as those used in this experiment. This will make the planning and execution of future campaigns much smoother.

Compared to previous systems, our system allows for a high degree of flexibility when it comes to resolution and scan patterns. However, as we have learned, everything is not perfect. Because the limited capability to estimate vertical velocities at low angles of elevation is most likely a generic problem with long-range WindScanner systems such as the one presented here, we support development of a hybrid system that also includes a short-range continuous-wave WindScanner, for example, in position for the RHI scanning WS3. This could then, at least locally, address the vertical wind component.

Although far from conclusive in the context of boundary layer meteorology and inhomogeneous surface characteristics, Fig. 7 serves as a good demonstration of how a system of WindScanners can be combined to study spatial variability of, for example, surface-layer winds. We believe that the system will serve as the backbone for new discoveries challenging classical theories, such as internal boundary layer theory, that are mostly based on relatively old campaigns involving only a few sparsely positioned anemometers (Bradley 1968).

Acknowledgments. We are grateful to the technical staff at Høvsøre test station. The corresponding author J. B. thanks the Carlsberg Foundation for financial support. N. V. is sponsored by the EC Marie Curie FP7-ITN-WAUDIT Project, Grant 238576. The work was partially supported by the Center for Computational Wind Turbine Aerodynamics and Atmospheric Turbulence under the Danish council for strategic research Grant 09-067216 and Windscanner.dk.

REFERENCES

Aitken, M. L., R. M. Banta, Y. L. Pichugina, and J. K. Lundquist, 2014: Quantifying wind turbine wake characteristics from scanning remote sensor data. *J. Atmos. Oceanic Technol.,* **31,** 765–787, doi:10.1175/JTECH-D-13-00104.1.

Bechmann, A., N. N. Sørensen, J. Berg, J. Mann, and P.-E. Réthoré, 2011: The Bolund Experiment, Part II: Blind comparison of microscale flow models. *Bound.-Layer Meteor.,* **141,** 245–271, doi:10.1007/s10546-011-9637-x.

Berg, J., J. Mann, and E. G. Patton, 2013: Lidar-observed stress vectors and veer in the atmospheric boundary layer. *J. Atmos. Oceanic Technol.,* **30,** 1961, doi:10.1175/JTECH-D-12-00266.1.

Bingöl, F., J. Mann, and D. Foussekis, 2009: Conically scanning lidar error in complex terrain. *Meteor. Z.,* **18,** 189–195, doi:10.1127/0941-2948/2009/0368.

——, ——, and G. C. Larsen, 2010: Lidar measurements of wake dynamics part I: One-dimensional scanning. *Wind Energy,* **13,** 51–61, doi:10.1002/we.352.

Bradley, E. F., 1968: A micrometeorological study of vertical profiles and surface drag in the region modified by a change in surface roughness. *Quart. J. Roy. Meteor. Soc.,* **94,** 361–379, doi:10.1002/qj.49709440111.

Browning, K. A., and R. Wexler, 1968: The determination of kinematic properties of a wind field using Doppler radar. *J. Appl. Meteor.,* **7,** 105–113, doi:10.1175/1520-0450(1968)007<0105:TDOKPO>2.0.CO;2.

Courtney, M., R. Wagner, and P. Lindelöw, 2008: Testing and comparison of lidars for profile and turbulence measurements in wind energy. *IOP Conf. Ser.: Earth Environ. Sci.,* **1,** 012021, doi:10.1088/1755-1315/1/1/012021.

Emeis, S., M. Harris, and R. M. Banta, 2007: Boundary-layer anemometry by optical remote sensing for wind energy applications. *Meteor. Z.,* **16,** 337–347, doi:10.1127/0941-2948/2007/0225.

Mann, J., 1994: The spatial structure of neutral atmospheric surface-layer turbulence. *J. Fluid Mech.,* **273,** 141–168, doi:10.1017/S0022112094001886.

Mayor, S. D., and E. W. Eloranta, 2001: Two-dimensional vector wind fields from volume imaging lidar data. *J. Appl. Meteor.,* **40,** 1331–1346, doi:10.1175/1520-0450(2001)040<1331:TDVWFF>2.0.CO;2.

Newsom, R., R. Calhoun, D. Ligon, and J. Allwine, 2008: Linearly organized turbulence structures observed over a suburban area by dual-Doppler lidar. *Bound.-Layer Meteor.,* **127,** 111–130, doi:10.1007/s10546-007-9243-0.

Peña, A., C. B. Hasager, S.-E. Gryning, M. Courtney, I. Antoniou, and T. Mikkelsen, 2009: Offshore wind profiling using light detection and ranging measurements. *Wind Energy,* **12,** 105–124, doi:10.1002/we.283.

——, S.-E. Gryning, J. Mann, and C. B. Hasager, 2010: Length scales of the neutral wind profile over homogeneous terrain. *J. Appl. Meteor. Climatol.,* **49,** 792–806, doi:10.1175/2009JAMC2148.1.

——, R. R. Floors, and S.-E. Gryning, 2014: The Høvsøre Tall Wind-Profile Experiment: A description of wind profile observations in the atmospheric boundary layer. *Bound.-Layer Meteor.,* **150,** 69–89, doi:10.1007/s10546-013-9856-4.

Sathe, A., and J. Mann, 2013: A review of turbulence measurements using ground-based wind lidars. *Atmos. Meas. Tech.,* **6,** 3147–3167, doi:10.5194/amt-6-3147-2013.

——, ——, J. Gottschall, and M. S. Courtney, 2011: Can wind lidars measure turbulence? *J. Atmos. Oceanic Technol.,* **28,** 853–868, doi:10.1175/JTECH-D-10-05004.1.

Smalikho, I. N., V. A. Banakh, Y. L. Pichugina, W. A. Brewer, R. M. Banta, J. K. Lundquist, and N. D. Kelley, 2013: Lidar investigation of atmosphere effect on a wind turbine wake. *J. Atmos. Oceanic Technol.,* **30,** 2554–2570, doi:10.1175/JTECH-D-12-00108.1.

Strang, G., 2005: *Linear Algebra and Its Applications*. 4th ed. Cengage Learning, 496 pp.

Trujillo, J.-J., F. Bingöl, G. Larsen, J. Mann, and M. Kühn, 2011: Light detection and ranging measurements of wake dynamics. Part II: Two-dimensional scanning. *Wind Energy,* **14,** 61–75, doi:10.1002/we.402.

Vasiljević, N., 2014: A time-space synchronization of coherent Doppler scanning lidars for 3D measurements of wind fields. Ph.D. thesis, Technical University of Denmark, 176 pp.

——, G. Lea, M. Courtney, J. Mann, and T. Mikkelsen, 2013a: The long-range WindScanner system—How to synchronously intersect multiple laser beams. *Proc. EWEA 2013 Conf.,* Vienna, Austria, EWEA, 457. [Available online at http://proceedings.ewea.org/annual2013/allfiles/634_EWEA2013presentation.pptx.]

——, ——, ——, J. Schneemann, D. Trabucchi, J.-J. Trujillo, R. Unguran, and J.-P. Villa, 2013b: The application layer protocol: Remote Sensing Communication Protocol (RSComPro). DTU Wind Energy E 0017 (EN), 43 pp.

Wyngaard, J. C., 2004: Toward numerical modeling in the ''terra incognita.'' *J. Atmos. Sci.,* **61,** 1816–1826, doi:10.1175/1520-0469(2004)061<1816:TNMITT>2.0.CO;2.

——, 2010: *Turbulence in the Atmosphere.* Cambridge University Press, 406 pp.